Acta Metallurgica Sinica (English Letters) (2022) 35:1837–1848
https://doi.org/10.1007/s40195-022-01413-7

Interfacial Oxides Evolution of High-Speed Steel Joints by Hot-Compression Bonding

Wei-Feng Liu[1,2] · Bi-Jun Xie[1] · Ming-Yue Sun[1] · Bin Xu[1] · Yan-Fei Cao[1] · Dian-Zhong Li[1]

Received: 10 January 2022 / Revised: 4 February 2022 / Accepted: 22 February 2022 / Published online: 21 May 2022
© The Chinese Society for Metals (CSM) and Springer-Verlag GmbH Germany, part of Springer Nature 2022

Abstract
The interfacial oxidation behavior of Cr4Mo4V high-speed steel (HSS) joints undergoing hot-compression bonding was investigated by using optical microscopy (OM), scanning electron microscopy (SEM), and transmission electron microscopy (TEM). In the heating and holding processes, dispersed rod-like and granular $\delta - Al_2O_3$ oxides were formed at the interface and in the matrix near the interface due to the selective oxidation and internal oxidation of Al, while irregular Si–Al–O compounds and spheroidal SiO_2 particles were formed at the interface. After the post-holding treatment, SiO_2 oxides and Si–Al–O compounds were dissolved into the matrix, and $\delta - Al_2O_3$ oxides were transformed into nanoscale $\alpha - Al_2O_3$ particles, which did not deteriorate the mechanical properties of the joints. The formation and migration of newly-formed grain boundaries by plastic deformation and post-holding treatment were the main mechanism for interface healing. The tensile test results showed that the strength of the healed joints was comparable to that of the base material, and the in-situ tensile observations proved that the fracture was initiated at the grain boundary of the matrix rather than at the interface. The clarification of interfacial oxides and microstructure is essential for the application of hot-compression bonding of HSSs.

Keywords Hot-compression bonding · High-speed steel · Interfacial oxides · Interface healing · Mechanical properties

1 Introduction

A high-speed steel (HSS) is a special tool steel with superior hardness and wear resistance, and is widely employed in the manufacturing of drills, dies, rolls, and cutting tools [1, 2]. The excellent mechanical properties of HSSs can be mainly attributed to the high contents of carbon and alloying elements [3], which have a significant impact on its weldability when employing conventional welding route [4]. The carbon equivalent value (CEV) of a steel is a critical index to evaluate the fusion weldability based on the International Institute of Welding (IIW) criteria, which is defined as:

$$\mathrm{CEV\ (wt\%)} = \mathrm{C} + (\mathrm{Mn}+\mathrm{Si})/6 + (\mathrm{Cr}+\mathrm{Mo}+\mathrm{V})/5 + (\mathrm{Ni}+\mathrm{Cu})/15 \quad (1)$$

According to the IIW, steels with CEV less than 0.4 wt% have superior weldability. However, the CEV of HSSs is typically much greater than 0.4 wt%, which implies that solidification cracks can occur at the fusion-welded joints due to the high residual stress induced during the formation of hard and brittle plate martensite in the cooling process [5, 6]. To solve this problem, careful pre-heating treatment and very strict control of the cooling rate are indispensable to prevent crack formation; however, this makes the fusion welding process complicated and even inappropriate for HSS [7, 8]. As a promising engineering material, the joining technique of HSSs is worth exploring to cope with this issue.

Owing to their advantages in welding work-pieces without local melting or microstructure disruption, several solid-state joining techniques have been recommended for the joining of HSSs, namely friction stir welding [9], diffusion welding [10], and hot-compression bonding [11]. Sahin et al. [12] joined

✉ Ming-Yue Sun
mysun@imr.ac.cn

✉ Dian-Zhong Li
dzli@imr.ac.cn

1 Shenyang National Laboratory for Materials Science, Institute of Metal Research, Chinese Academy of Sciences, Shenyang 110016, China

2 School of Materials Science and Engineering, University of Science and Technology of China, Shenyang 110016, China

S6-5-2 HSS and AISI 1040 medium-carbon steel via friction stir welding. The tensile strength of the joints increased with increasing friction pressure and time, reaching the maximum value of approximately 75% that of base medium-carbon steel and 65% that of base HSS. Post-weld annealing (650 ℃ for 4 h) is essential to alleviate the brittleness of joints to some degree. Mahmoudiniya et al. [13] investigated the microstructure and mechanical properties of butt welds under different transverse speeds. Nevertheless, friction stir welding is more appropriate for sheet products owing to its limited penetration depth [14]. Shen et al. [4] investigated the effects of diffusion bonding temperature, pressure, and time on the microstructure evolution and tensile strength of powder metallurgy HSSs; they demonstrated that a complete weld can be obtained at a temperature of 1100 ℃ within varied ranges of the pressure and time. However, Yang et al. [15] and Mo et al. [16] stated that conventional diffusion bonding requires a high machining accuracy for the surfaces to be bonded, relatively high pressure, and long dwell time; this makes it a high energy-consuming and inefficient process.

Hot-compression bonding is a rapid solid-state joining technology characterized by high temperature and plastic deformation [17], making it particularly suitable for parts with large sections. Sun et al. [18] reported the manufacturing of a large-scale stainless steel forging ring (ϕ15.6 m) by multilayer additive hot-compression bonding technology. The interfacial quality is a key issue in hot-compression bonding [19]. Various studies have been conducted on the evolution and complete healing of bonding interfaces [20, 21]. Zhang et al. [22] attributed void closure to the plastic flow, interface diffusion, and volume diffusion around the voids in the bonding of stainless steel. Zhang et al. [23] and Zhou et al. [24] investigated the interfacial dynamic recrystallization (DRX) of IN718 and ODS joints, respectively. As hot-compression bonding is typically conducted at high temperatures, i.e., lower than the melting point of base materials, oxides are inevitably formed at the interface due to the limited vacuum degree, particularly in metals with elements that can easily form oxides [25]. With the increase in the deformation strain, the virginal material is exposed as the interfacial oxide film is broken [26]. Nevertheless, the regions where interfacial oxides exist are typically the preferential cracking sites, which significantly deteriorates the tensile and shear properties of joints [27]. Xie et al. [28] found that the decomposition of interfacial oxides ($MnCr_2O_4$) is beneficial to the recovery of the mechanical properties of the stainless steel bonding joints. The thermodynamic stability and decomposition mechanism of $MnCr_2O_4$ were also studied by combining first-principle calculations with the thermodynamics approach [29]. However, Wang et al. [30] found that the impairing effect of the oxides on the joints can be largely minimized when the oxide fragments are enwrapped in the metal matrix. Despite its potential for solid-state joining, the hot-compression bonding of HSSs has rarely been reported, and the effect of interfacial oxides on the joint performance of HSSs is unclear.

In this work, the hot-compression bonding of Cr4Mo4V HSS was first conducted, followed by a post-holding treatment to promote interface healing. The formation and evolution of interfacial oxides and their effect on the mechanical properties were investigated. The tensile strength and fracture behavior of the joints were studied by in-situ and in-situ testing, respectively. Finally, the healing mechanism of the hot-compression bonding interface of the HSS was analyzed based on the experimental results.

2 Experimental

2.1 Materials and Hot-Compression Strategy

A commercial Cr4Mo4V HSS, received in the annealed state, was used as the raw material in the hot-compression process. Table 1 presents its chemical composition. The microstructure of the as-received Cr4Mo4V steel comprises a typical ferritic matrix and significant amounts of primary and secondary carbides [31], as shown in Fig. 1a. The contacting surfaces of the irregular cylindrical samples for bonding were wet-ground and ultrasonically cleaned. The hot-compression process was conducted in a thermal simulator machine. To explain the effect of oxides on the interfacial healing, a vacuum degree of 1.0×10^{-1} torr was applied to obtain more oxides for the hot-compression test, which is the lowest allowed value for the thermal simulator machine. The temperature of the joint was recorded using K-type thermocouples welded to the sample surface (Fig. 1b). After assembling coaxially using a clamp kit, the samples were heated to 1150 ℃ at a heating rate of 5 ℃/s and maintained at this temperature for 5 min to eliminate any temperature gradient. The samples were then compressed isothermally at a strain rate of 0.1 s^{-1} until the engineering strain reached 30%. After isothermal compression, the samples were cooled to the ambient temperature in a vacuum chamber. To investigate the effect of post-holding treatment on the microstructural evolution of the bonding interface, the as-compressed samples were divided into several groups and sealed in vacuum tubes (7.6×10^{-6} torr). The sealed samples

Table 1 Chemical composition of commercial Cr4Mo4V steel (wt%)

C	Cr	Mo	V	Si	Al	Fe
0.82	4.20	4.24	1.01	0.21	0.016	Bal.

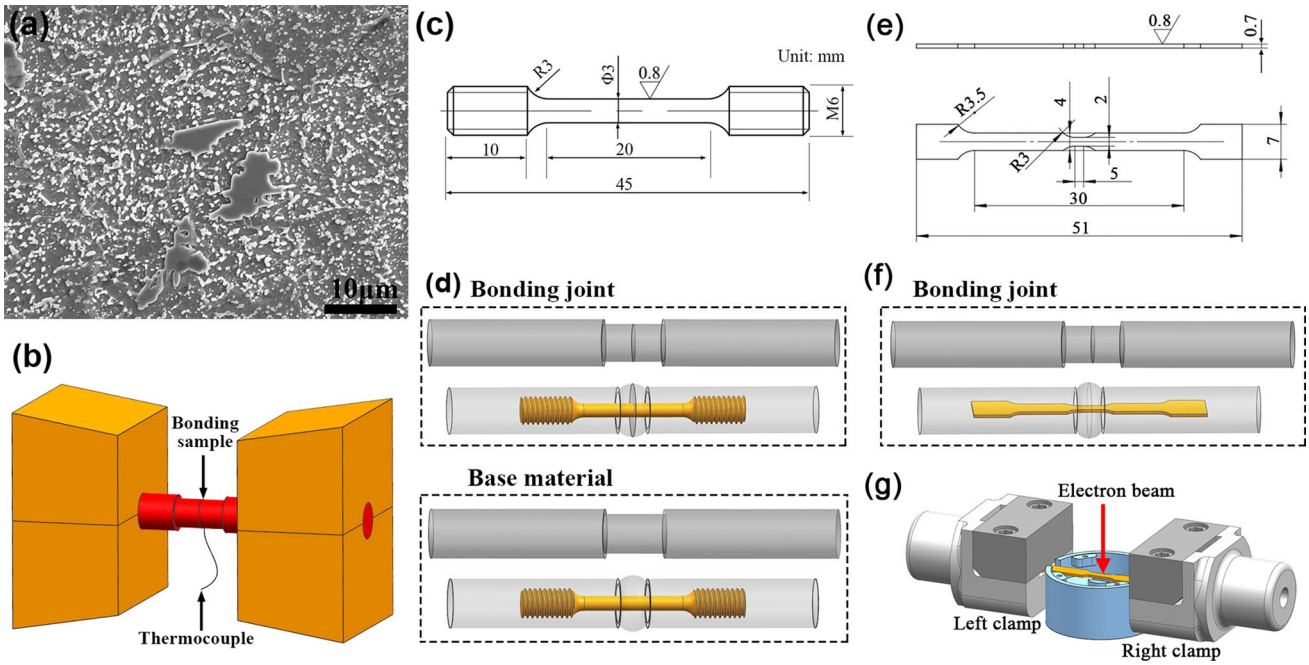

Fig. 1 **a** Microstructure of the as-received Cr4Mo4V HSS, **b** schematic of hot-compression bonding tests conducted using the thermal simulator machine, **c** dimensions of tensile test samples, **d** sampling scheme of tensile specimens from the bonding joint and base material, **e** dimensions of in-situ tensile test specimens, **f** sampling scheme of in-situ tensile specimens from the bonding joint, **g** schematic of the in-situ SEM setup for the tensile test

were held for 10 min, 1 h, 6 h, 12 h, and 24 h at 1150 ℃ in a muffle furnace.

2.2 Analysis Methods

After the post-holding treatment, the samples were cut along the center section parallel to the compression direction, and the original bonding interface area was then mechanically ground, polished, and chemically etched in a 10% nitric acid/alcohol solution. The interfacial microstructure was observed using a Zeiss MC63 optical microscope (OM) and an FEI Inspect F50 scanning electron microscope (SEM) along with energy dispersive X-ray spectroscopy (EDS). The interfacial oxides were identified using FEI Talos F200X equipped with an EDS instrument. The TEM samples containing interfacial oxides were prepared using focused ion beam (FIB; Helios NanoLab 600, FEI) with the in-situ lift-out method, as shown in Fig. 2.

Accordingly to the Standard GB/T228-2010, the dog-bone-shaped tensile specimens were directly processed from the as-compressed and post-holding-treated samples. A tensile specimen from the base material was designed for comparison with that from the bonding joints. Figure 1c and d shows schematics of the dimensions and locations of the tensile specimens, respectively. Tensile tests were conducted using an AG-100KNG machine at a strain rate of 0.1 mm/

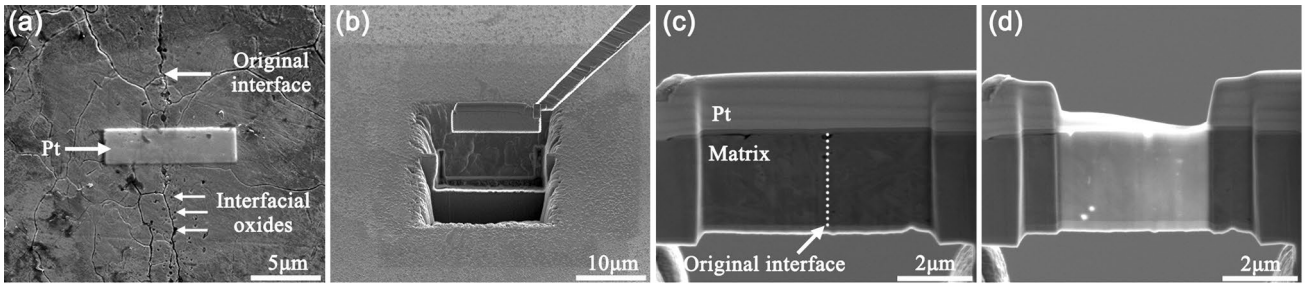

Fig. 2 Main procedures in the FIB lift-out technique for TEM sample preparation: **a** Pt is deposited at the interface area, **b** foil containing the interface area is cut free with the base material and lifted out of the sample, **c** foil is welded on a Cu grid, **d** foil is further thinned to electron transparency by ion milling

min. To study the fracture behavior of samples containing an interface, in-situ tensile tests were performed in an FEI OUANTA FEG650 SEM. Tensile samples with dimensions of 51 mm × 7 m × 0.7 mm (Fig. 1e) were extracted from the bonding joint, as illustrated in Fig. 1f. Before testing, a 51 mm × 7 mm face was mechanically ground, polished, and etched using Nital to observe the fracture phenomenon clearly. Figure 1g shows the in-situ tensile setup, where the left- and right-side clamps were controlled by a multistep gear-drive system to ensure biaxial stretching along the central axis. The tensile loading rate was 1 μm/s, and SEM images were captured during pauses in the tensile process.

3 Results

3.1 Interfacial Microstructure of As-compressed Bonding Joints

The initial microstructure of the Cr4Mo4V HSS before hot-compression was investigated. The assembled samples were manually separated without deformation after holding at 1150 °C for 5 min; Fig. 3 shows the microstructure of the contacting surface. The honeycomb-like microstructure indicates a weak diffusion weld between the assembled parts during the heating and holding processes. A few crater-like holes embedded with the oxides can be observed on the contacting surface. From the EDS mapping, the oxides are found to be rich in Al or Si elements, which are marked by yellow and red circles, respectively. Overall, the oxides appear as separated particles rather than continuous films.

Figure 4 shows the profile of the as-compressed bonding interface. Discontinuous and dispersed oxide particles were found along the original interface, which can be divided into three categories, namely Si–oxides, Al–oxides, and Si–Al–O compound oxides (as indicated in the inset of Fig. 4a). The large and spheroidal Si-oxides mainly exist at the interface. The Al-oxides appearing as rod-like and granular particles mainly exist at the interface and in the matrix near the interface, so do the large and irregular Si–Al–O compound oxides. A TEM experiment was conducted to analyze the composition and structure of the interfacial oxides. As shown in Fig. 5, the atomic ratio of Al and O in the Al–oxide is approximately 2:3, while the atomic ratio of Si and O in the Si–oxide is approximately 1:2. Combined with the selected-area electron diffraction pattern (inset in Fig. 5a) and the high-resolution TEM (inset in Fig. 5c), the Al–oxide is eventually identified as $\delta - Al_2O_3$, while the Si–oxide is

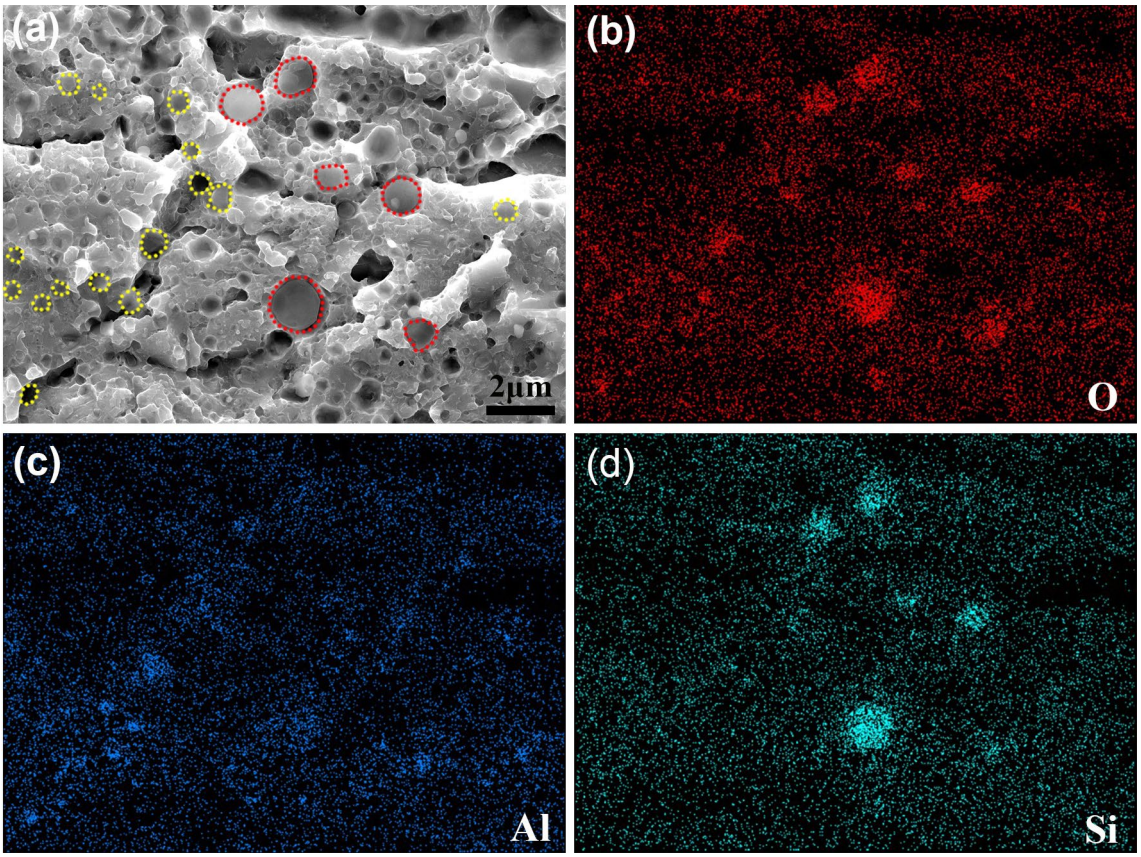

Fig. 3 **a** Micrograph of the bonding interface before hot-compression, **b-d** elemental distributions of O, Al, and Si, respectively

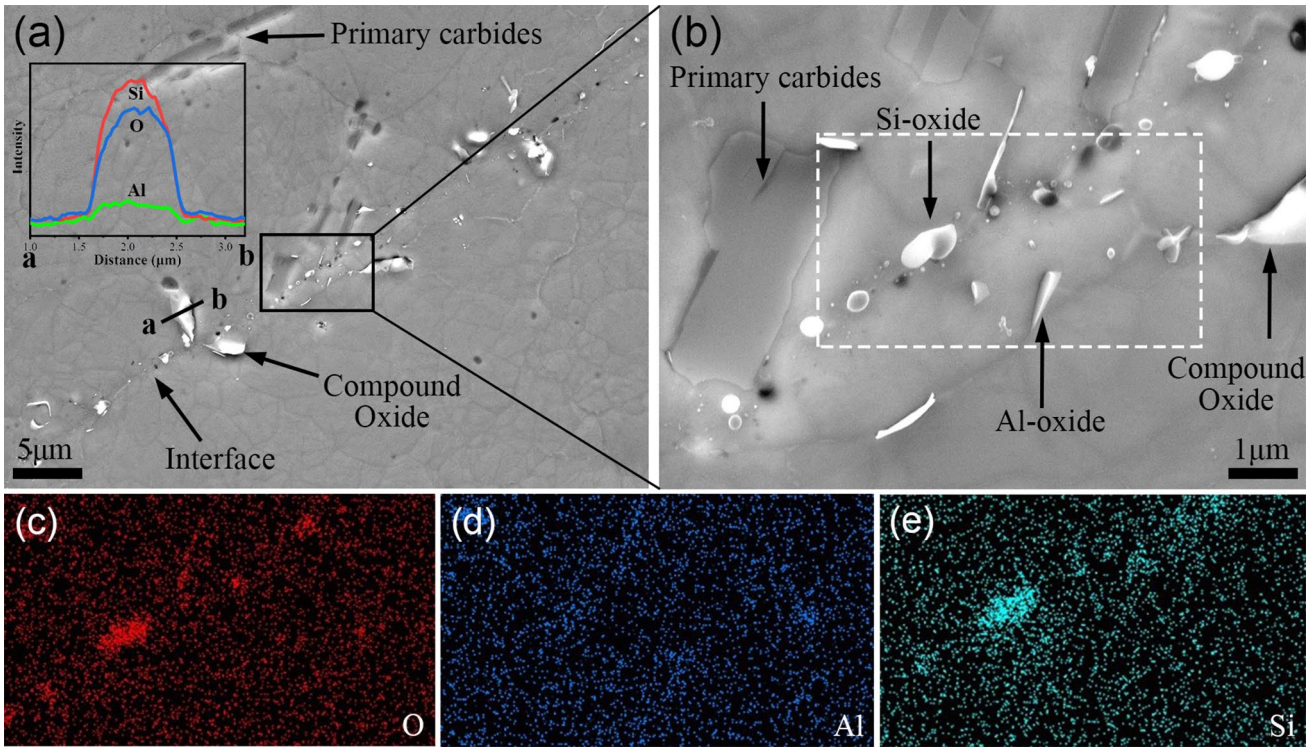

Fig. 4 **a** and **b** Oxides at the original bonding interface, and EDS maps of **c** O, **d** Al, **e** Si in the white rectangle

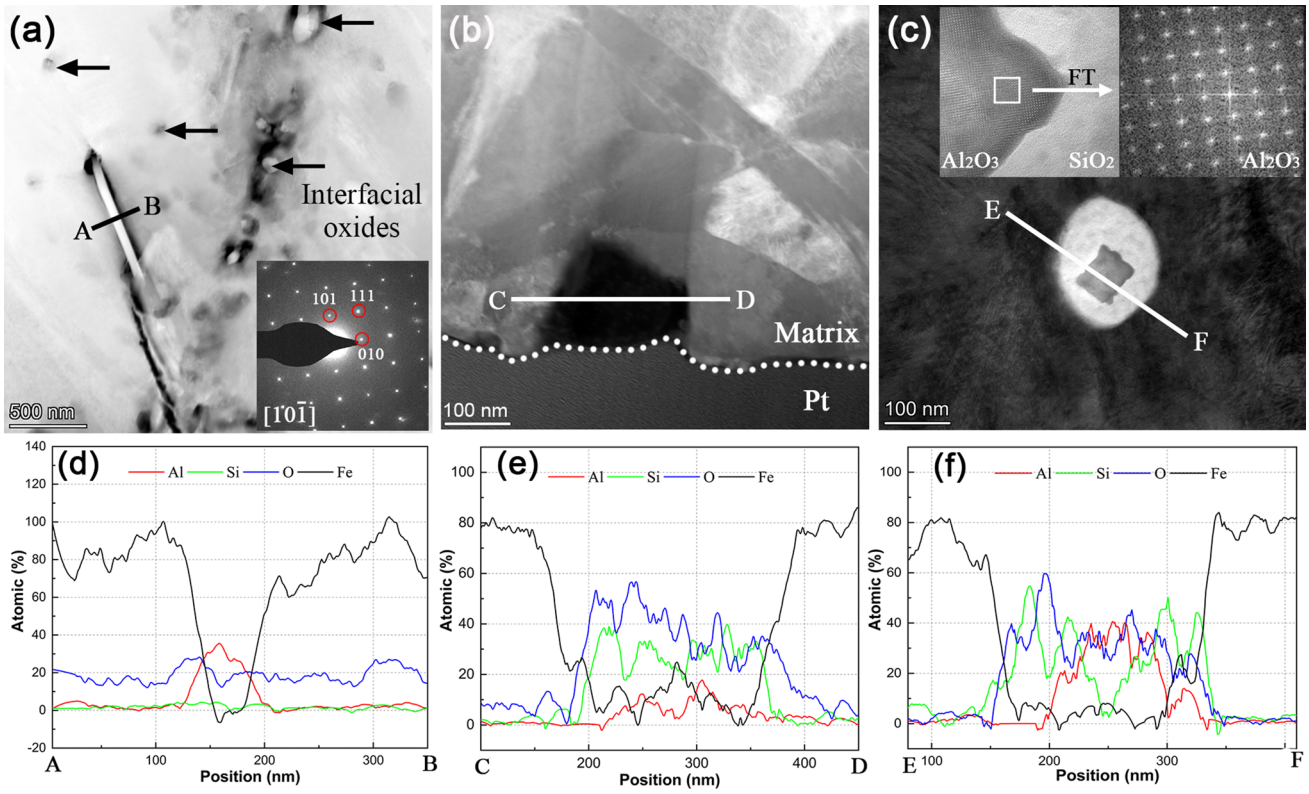

Fig. 5 TEM images of interfacial oxides: **a** Al_2O_3, **b** SiO_2, and **c** compound oxide. EDS profiles of oxides: **d** Al_2O_3, **e** SiO_2, **f** compound particles. FT: Fourier transformation

identified as amorphous SiO_2 (Fig. 5b and e). In addition, nanoscale compound oxides comprising inner $\delta - Al_2O_3$ and outer SiO_2 can be found at the interfacial area (Fig. 5c and f).

3.2 Evolution of Interfacial Microstructure and Oxides During Post-holding Process

Figure 6 shows the interfacial microstructures of the samples under different post-holding times at 1150 ℃. In the as-compressed state (Fig. 6a), the two samples exhibited a completely physical contact as the interface is a curved line (as indicated in the inset). The austenite grains were largely refined in the deformation process, resulting in recrystallization in both the matrix and the interfacial area. The oxides along the interface were too small to distinguish at the macroscale. After holding for 10 min, the grains grew rapidly, and some of the interfacial grains bulged into the opposite site, leaving a black string at the grain interior, as indicated by white arrows. As the holding time was increased to 1 h and 6 h, the grains further grew as more proportions of the interface were replaced by the bulged grains. For holding times of 12 h and 24 h, the original interface was completely replaced by the bulged grains. At the microscale, there is a black string comprising oxides at the initial interface.

The interfacial oxides are further studied by SEM in Fig. 7 and TEM in Fig. 8. A significant amount of oxide particles remained along the bonding interface in the as-compressed state, and the matrix among oxides contacted to form new grain boundaries. After holding for 10 min, the interfacial spheroidal SiO_2 oxides were dissolved into the matrix, while the irregular Si–Al–O compound oxides and rod-like and granular $\delta - Al_2O_3$ oxides showed little change. When the holding time increased to 1 h, most of the large and irregular Si–Al–O compound oxides disappeared leaving only $\delta - Al_2O_3$ oxides corresponding to the black string shown in Fig. 6. As the holding time prolonged to 24 h, the amount of residual Al_2O_3 oxides was further reduced. Notably, the distribution of the residual Al_2O_3 inside the bulged grains was maintained at the original interface without evident movement. Finally, only refined nanoscale Al_2O_3 particles remained at the grain interior in the original interfacial area, identified as $\alpha - Al_2O_3$ oxides, as presented in Fig. 8.

3.3 Mechanical Properties

Tensile tests were conducted to evaluate the bonding strength of the joints. Generally, it is inappropriate to evaluate the bonding degree using the absolute strength of joints because samples with different thermal histories have different tensile strengths. The restoration ratio (σ) of the tensile strength was used to assess the bonding degree of the samples and is defined as follows:

$$\sigma = \frac{R_{mj}}{R_{mb}} \times 100\% \tag{2}$$

where R_{mj} is the tensile strength of a hot-compressed joint, and R_{mb} is the tensile strength of the base material under the same compression and holding conditions. As presented in Fig. 9, the tensile strengths of the as-compressed bonding

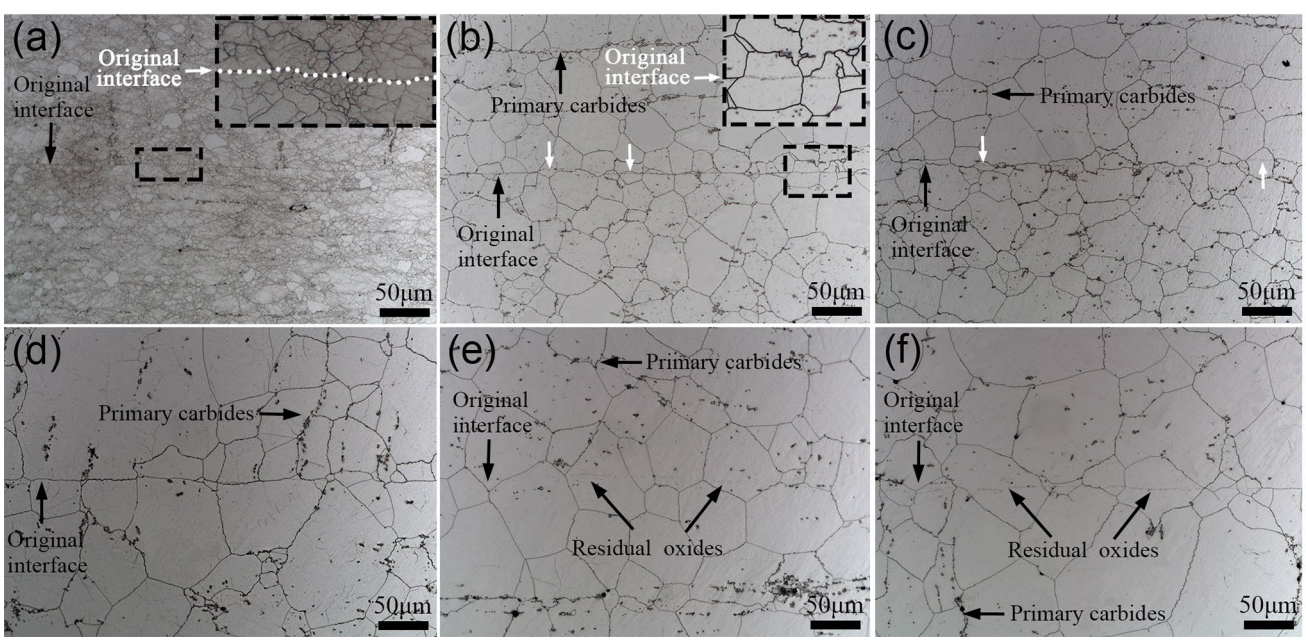

Fig. 6 Evolution of the interfacial microstructure under different holding time: **a** 0 min, **b** 10 min, **c** 1 h, **d** 6 h, **e** 12 h, **f** 24 h

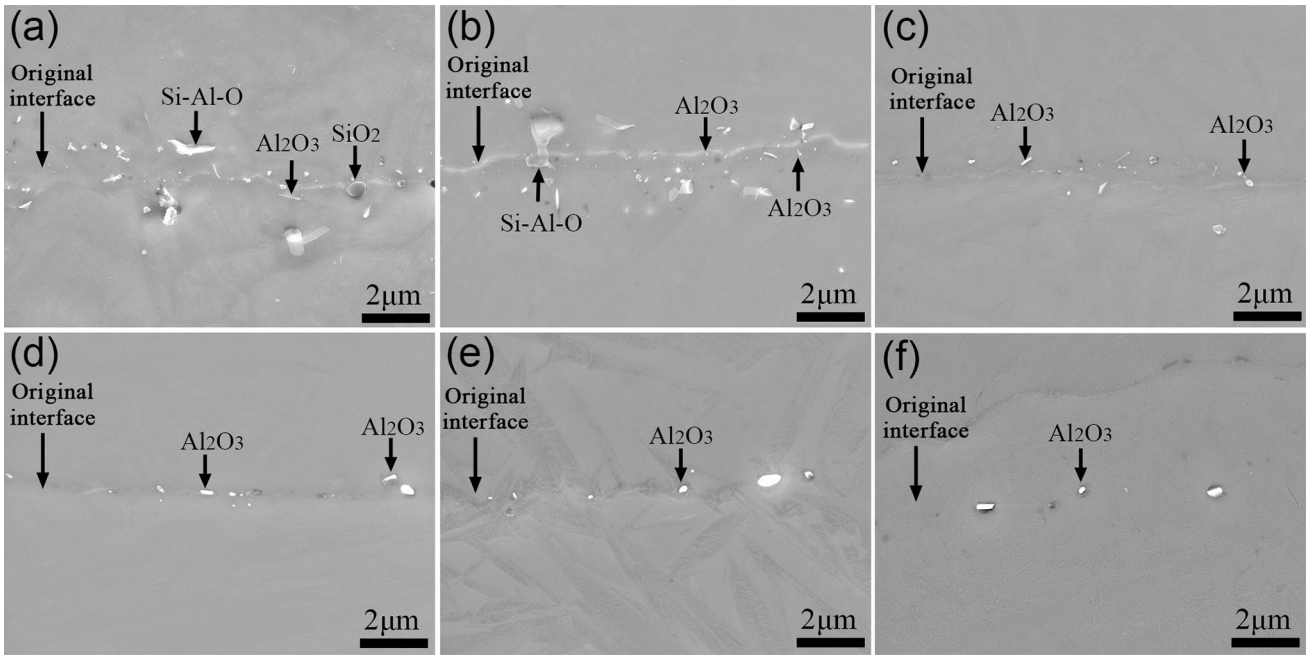

Fig. 7 Evolution of interfacial oxides under different holding time: **a** 0 min, **b** 10 min, **c** 1 h, **d** 6 h, **e** 12 h, **f** 24 h

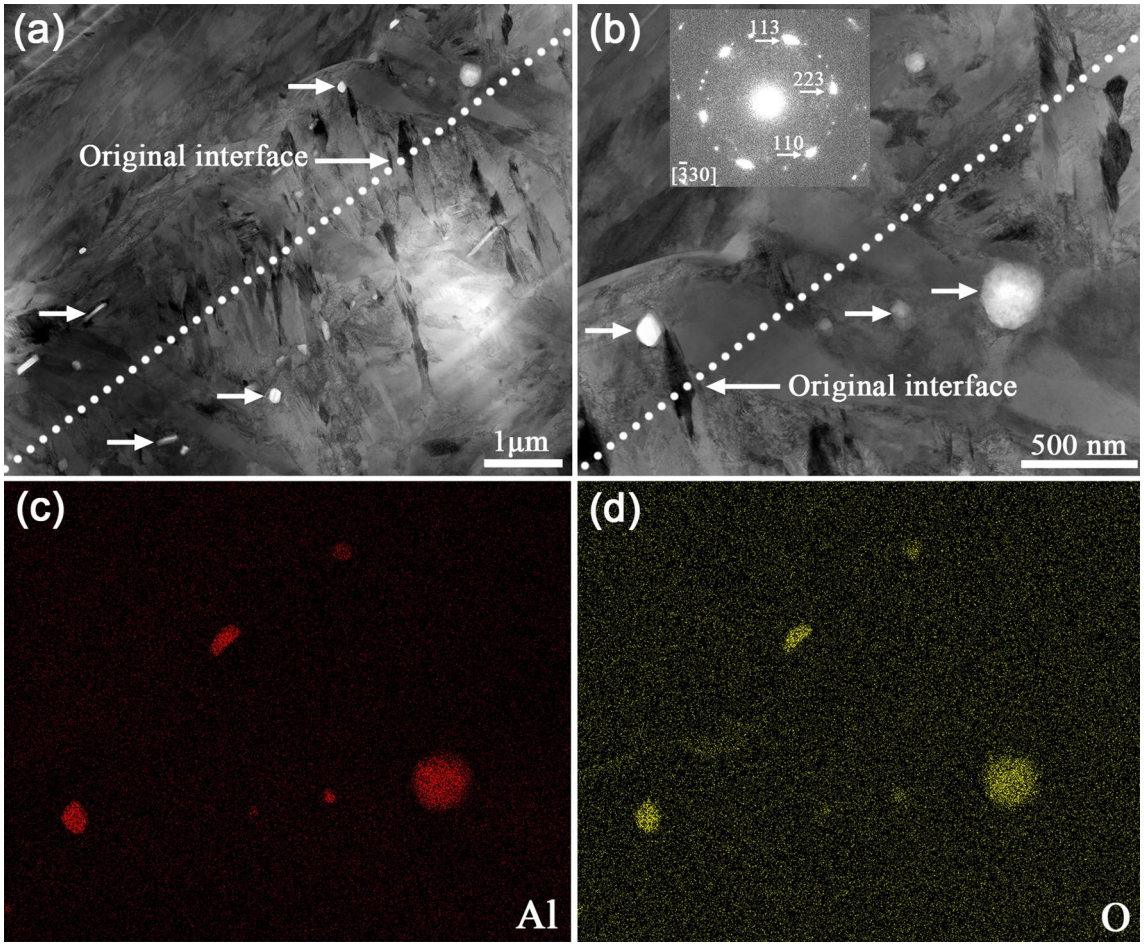

Fig. 8 **a** and **b** TEM images of interfacial oxides after 24 h of holding at 1150 ℃. EDS maps of **c** Al **d** O in image **b**

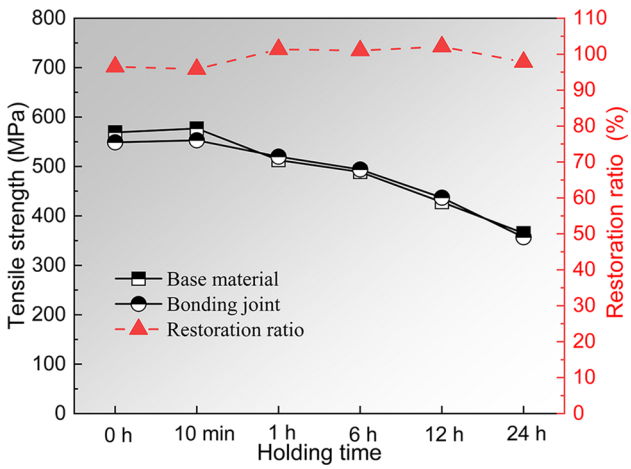

Fig. 9 Tensile strengths of the bonding joints and base material under different holding time

joint and base material are 549 MPa and 569 MPa, respectively, and the restoration ratio is 96.49%. The comparable tensile strengths indicate that the bonding interface was nearly healed after deformation under the 1150 ℃/30% condition. With the holding treatment, the restoration ratio of the joints increased to nearly 100%. The tensile strength of the base material and bonding joints both slightly decreased with increasing holding time, which is attributed to grain coarsening. Figure 10 shows the tensile fracture morphologies of the bonding joints and base materials, where no oxides can be found on the fracture image due to the small size and limited amount. The samples underwent brittle fracture, and all the surfaces showed intergranular or transgranular features, proving that the joint exhibited nearly the same fracture behavior as the base material.

At the macroscale, the fracture zone of the dog-bone-shaped tensile samples was mainly located at the substrate. In-situ tensile testing was conducted to analyze the fracture behavior; Fig. 11 shows the microstructural evolution of samples containing an interface. It is challenging to identify the interfacial nanoscale $\alpha - Al_2O_3$ oxides due to the low magnification. The original interface of the sample subjected to 24 h of holding was distinguished at the middle of the micrograph based on the grain size difference (Fig. 11a). When the tensile displacement increased to 186 μm, a crack initiated at the grain boundary on one side rather than in the original interface area in Fig. 11b. The crack propagated rapidly along the grain boundary with increasing displacement (Fig. 11c). Finally, the sample fractured immediately at the matrix in a brittle model, as shown in Fig. 11d.

4 Discussion

4.1 Formation and Dissolution of Interfacial Oxides

After cleaning the contaminant layer and oxide scale on the surface by mechanical grinding, the initial bonding interface before heating is clean and fresh. However, due to the limited vacuum degree (1.0×10^{-1} torr), the oxidation of

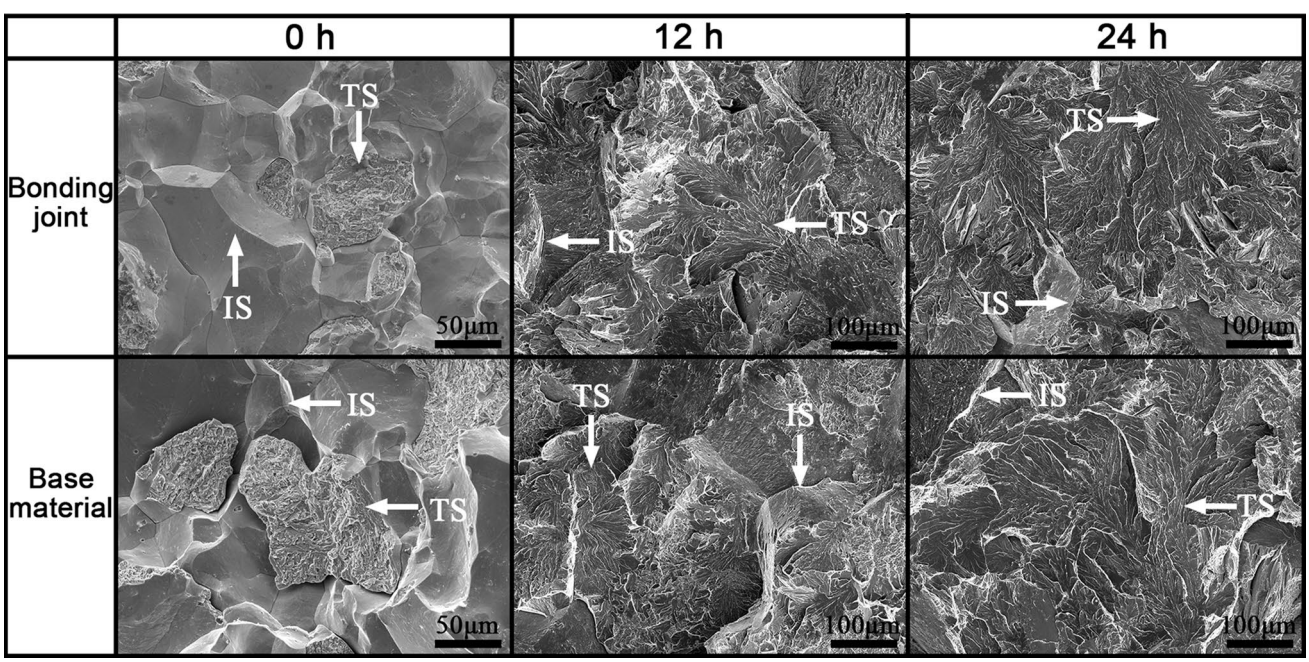

Fig. 10 Tensile fracture morphologies of the bonding joints and base material under various deformation and holding time. IS: intergranular surface, TS: transgranular surface

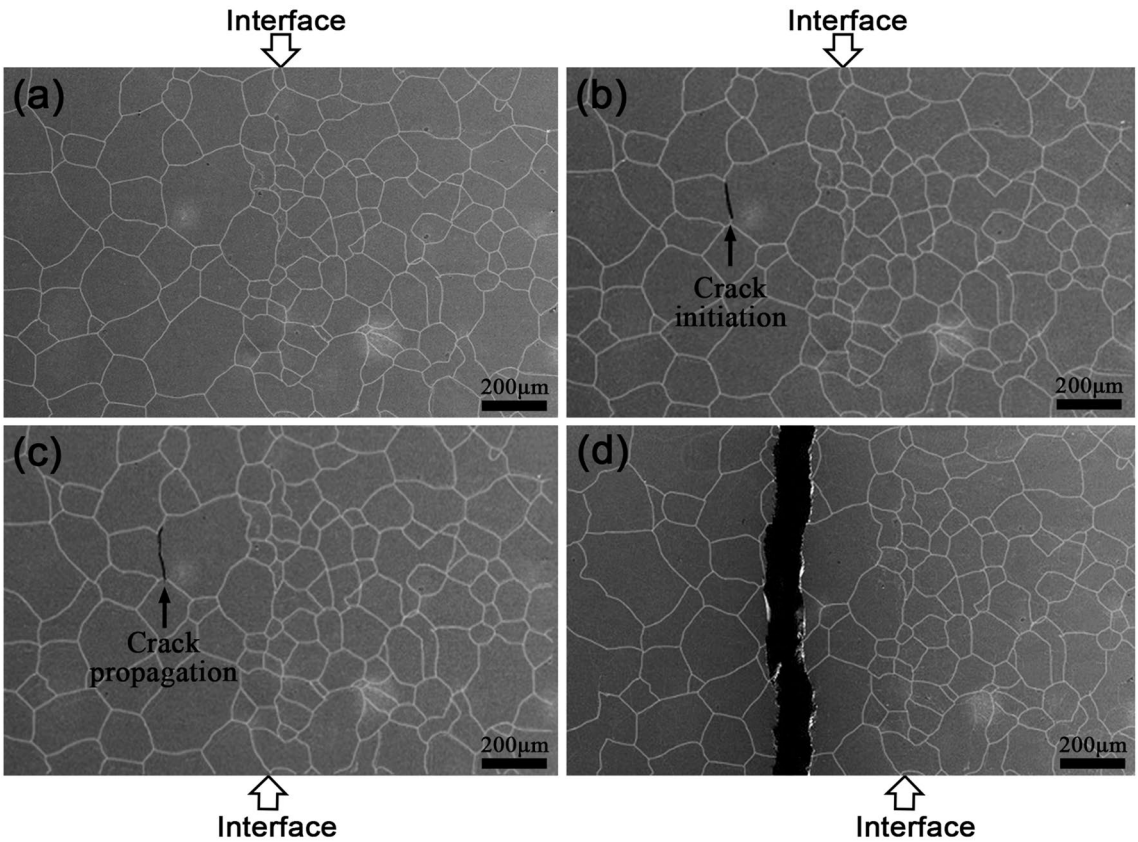

Fig. 11 In-situ tensile observations of the microstructural evolution of bonding joints with displacements of **a** 0 μm, **b** 186 μm, **c** 197 μm, **d** 245 μm

the alloying elements during the heating and holding processes is inevitable, particularly for elements that can easily form oxides, which is a selective oxidation process [32]. The oxidation potential of the various alloying elements in this process depends on the standard molar Gibbs free energy ($\Delta_r G_m^\theta$). According to the Gibbs–Helmholtz formula, $\Delta_r G_m^\theta(T)$ is calculated as:

$$\Delta_r G_m^\theta(T) = \Delta_r \vec{H}_m^\theta(T) - T\Delta_r S_m^\theta(T) \tag{3}$$

$$\Delta_r H_m^\theta(T) = \Delta_r H_m^\theta(298.15\ \mathrm{K}) + \int_{298.15\mathrm{K}}^{T} \Delta_r C_{p,m} \mathrm{d}T \tag{4}$$

$$\Delta_r S_m^\theta(T) = \Delta_r S_m^\theta(298.15\mathrm{K}) + \int_{298.15\mathrm{K}}^{T} \frac{\Delta_r C_{p,m}}{T} \mathrm{d}T \tag{5}$$

where $\Delta_r H_m^\theta(T)$ is the standard molar enthalpy, $\Delta_r S_m^\theta(T)$ is the standard molar entropy, $\Delta_r C_{p,m}$ is the standard molar heat capacity at constant pressure, and T is the temperature in Kelvin. Table 2 presents the corresponding thermodynamic parameters of the molecular formulae of the various oxides [33]. The standard molar reaction Gibbs function ($\Delta_r G_m^\theta$) of the various oxides at 1150 ℃ (1423.15 K) was calculated and listed in Table 2 based on Eqs. (3–5). When the temperature reaches 1150 ℃, $\Delta_r G_m^\theta$ of the various oxides follows the order: $Al_2O_3 < SiO_2 < Cr_2O_3 < FeO < Fe_3O_4 < Fe_2O_3$. In the heating and holding processes, the Al element has the strongest affinity with the O element compared with the other alloying elements; it firstly reacts with O and forms $\delta - Al_2O_3$ particles and whiskers.

As observed from the profile of the interface in Fig. 4a and b, the rod-like and granular $\delta - Al_2O_3$ oxides mainly exist at not only the interface but also in the matrix near the interface. According to the internal oxidation theory, the diffusion of O atoms from the interface to the matrix is easier than the outward diffusion of Al atoms [34]. The internal oxidation of the solute elements facilitated by the diffusion of O atoms from the surface scale results in subscale formation of $\delta - Al_2O_3$ particles. Due to the low amount of Al (0.016 wt%) in the matrix, a part of O reacted with the other alloying elements. From $\Delta_r G_m^\theta$ in Table 2, Si has the second strongest affinity with O. After the complete consumption of Al atoms at the interface, the Si atoms at the interface reacted with the O atoms. The SiO_2 oxides were only formed at the interface because

Table 2 Corresponding thermodynamic parameters of various chemical reactions at 298.15 K and 1423.15 K

Chemical reaction	$\Delta_r H_m^\theta$ (kJ · mol^{-1}) (298.15 K)	$\Delta_r S_m^\theta$ (J · mol^{-1} · K^{-1}) (298.15 K)	$\Delta_r H_m^\theta$ (kJ · mol^{-1}) (1423.15 K)	$\Delta_r S_m^\theta$ (J · mol^{-1} · K^{-1}) (1423.15 K)	$\Delta_r G_m^\theta$ (kJ · mol^{-1}) (1423.15 K)
$2Fe(s)+O_2(g)=2FeO(s)$	−533,000	−151.7	−507,462	−116.2	−342,064
$6FeO(s)+O_2(g)=2Fe_3O_4(s)$	−637,800	−236.3	−693,036	−313.1	−247,532
$4Fe_3O_4(s)+O_2(g)=6Fe_2O_3(s)$	−471,600	−266.3	−449,190	−235.1	−114,552
$4/3Cr(s)+O_2(g)=2/3Cr_2O_3$	−759,800	−182.7	−738,837	−153.6	−520,279
$Si(s)+O_2(g)=SiO_2(s)$	−903,500	−177	−909,012	−184.7	−646,213
$4/3Al(s)+O_2(g)=2/3Al_2O_3(s)$	−1,117,800	−208.9	−1,127,962	−223.0	−810,571

the O atoms diffusing into the matrix easily react with Al. Moreover, large and irregular Si–Al–O compound oxides were formed in this selective oxidation process. The TEM analysis of the compound oxides in Fig. 5c demonstrates that the oxidation of Al is prior to Si as $\delta-Al_2O_3$ oxide particles act as nucleation sites of SiO_2 oxides. Overall, unlike the continuous and thick oxide film formed at the hot-compressed interface of stainless steel [26], the interfacial oxides of Cr4Mo4V HSS, namely $\delta-Al_2O_3$ and SiO_2, are discontinuous and dispersed. The discontinuous distribution of the oxides is beneficial for interface healing because the virginal matrix can contact directly without extrusion from the continuous and dense oxide films [14].

In the deformation process, the interfacial oxides were surrounded by the matrix and transformed into intragranular inclusions. The evolution of these oxides during the holding process in the enclosed environment mainly depends on the thermodynamics of the matrix and oxides. According to Xie et al. [35], the interfacial oxides ($MnCr_2O_4$) of stainless steel joints decompose during holding due to the lower equilibrium oxygen partial pressure (P_{O_2}) of the matrix. The decomposition product oxygen ions diffuse inward from the interface and react with the solute metal to form Al_2O_3 oxides [36]. This helps explain the dissolution behavior of the interfacial oxides in Cr4Mo4V HSS joints. The activity of the O element in the Cr4Mo4V steel matrix was calculated using Thermo-Calc software with TCFE8 database. As presented in Fig. 12, the activity of O element in the matrix at 1150 ℃ is 1.73×10^{-17}, and the corresponding equilibrium oxygen partial pressure (P_{O_2}) is 1.61×10^{-37} atm. Typically, it is difficult to form native SiO_2 inclusions in the matrix under such low P_{O_2} [35]. The SiO_2 oxides, formed in the heating and holding processes when the P_{O_2} was high, were unstable after they transformed into intragranular inclusions in the hot-compression process. Therefore, the SiO_2 oxides would rapidly decompose into metallic ions and oxygen ions after holding for 10 min at 1150 ℃. The large and irregular Si–Al–O compound oxides with a high Si content gradually dissolved into the matrix with prolonged holding time. There were only $\delta-Al_2O_3$ oxides at the interface after 1 h of holding.

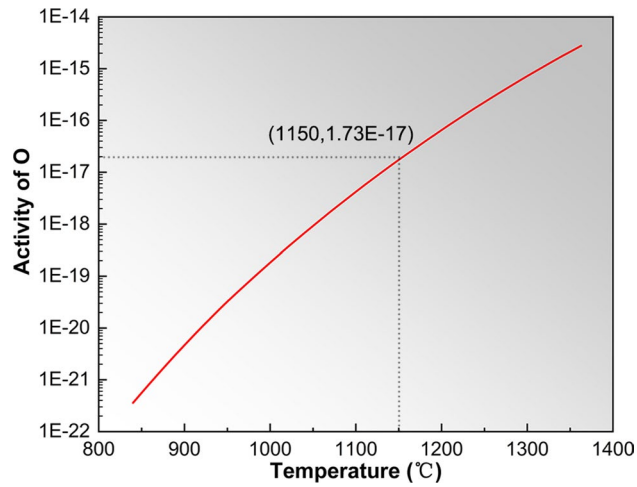

Fig. 12 Activity of O element in the Cr4Mo4V steel matrix versus the temperature

The long holding time results in the transformation of transitional $\delta-Al_2O_3$ to stable $\alpha-Al_2O_3$ oxides, and the latter is at the nanoscale and cannot dissolve into the matrix despite the long holding time (Fig. 7f). The transformation of $\delta-Al_2O_3\rightarrow\alpha-Al_2O_3$ has been reported in the literature for other materials [37]. Belonoshko et al. [38] reported that high temperature and free surfaces can contribute to the transition from metastable Al_2O_3 to thermodynamically-stable $\alpha-Al_2O_3$. Chen et al. [39] calculated the energy of Al_2O_3 with different structures and found that the total energy of $\alpha-Al_2O_3$ (−1431.86 eV) is lower than that of $\delta-Al_2O_3$ (−1430.18 eV), which indicates that $\delta-Al_2O_3$ can be converted to $\alpha-Al_2O_3$ during post-holding process. Therefore, only a black string comprising nanoscale $\alpha-Al_2O_3$ oxides remains at the original interface of Cr4Mo4V joint, as illustrated in Fig. 13e.

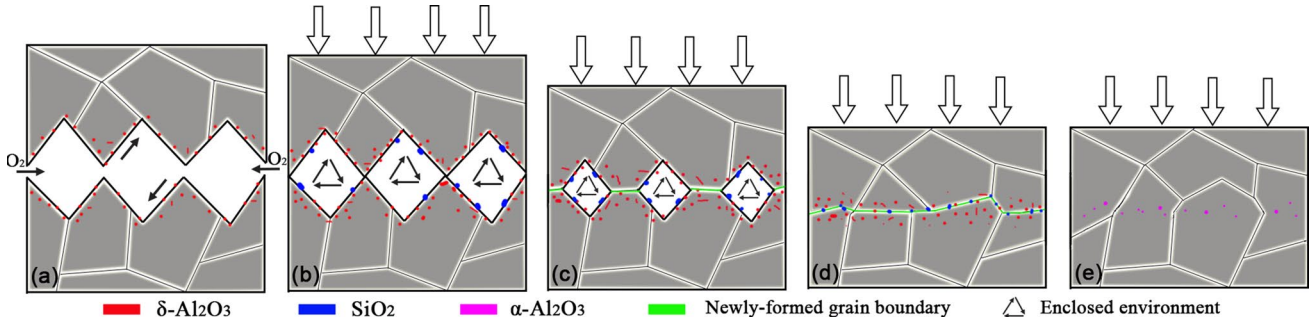

Fig. 13 Schematics of the healing mechanism of hot-compression bonding interface

4.2 Healing Mechanism of Bonding Interface

Figure 13 shows the healing mechanism of the Cr4Mo4V HSS bonding interface. The initial interface comprising convex and concave sections is rather irregular. In the heating and holding processes, dispersed $\delta - Al_2O_3$ and SiO_2 particles are successively formed at the interface and in the matrix near the interface (Fig. 13a and b). In the deformation process, the protruded sections are in direct contact and transform into new grain boundaries, as indicated in green in Fig. 13c. According to Kizuka [40], the atoms on the surface of metals contact spontaneously and transform into new grain boundaries when the surfaces approach the critical distance, i.e., a few atoms apart. The plastic deformation of interfacial materials during hot compression can produce atomic-level contact areas, which transform the interface into new grain boundaries, resulting in a metallurgical bonding. Notably, the hindering effect of oxides on the exposure and contacting of virginal material in Cr4Mo4V steel joints is negligible because of the discontinuous and dispersed distribution, making it easy to form new grain boundaries at a low deformation strain.

With increasing strain, more interfacial areas come in contact and transform into new grain boundaries. Meanwhile, interfacial oxides with different morphologies are completely transformed into inclusions in the matrix (Fig. 13d). The tensile testing results, shown in Fig. 9, demonstrate that the effects of discontinuous oxide particles surrounding the matrix on the mechanical properties are negligible because of their fine size and limited amount. Similar results have also been reported for stainless steel joints [29] and In718 superalloy joints [31]. In the holding process, the newly-formed grain boundaries can migrate to the opposite side, leading to enhanced interpenetration of the interfacial grains. The hot-compression can produce many movable dislocations near the interfacial grain boundaries via severe plastic deformation [17]. The stored energy generated by the dislocations can act as the driving force of the grain boundary migration during the holding process. Finally, the original interface is completely replaced by the migrated grains (Fig. 13e). The in-situ tensile testing results show that the healed interface has a comparable strength to the matrix as the crack initiates at one side of the joint.

5 Conclusions

The interfacial microstructure and oxides of Cr4Mo4V HSS joints subjected to hot-compression and post-holding treatment was investigated. The main results are as follows:

1. In the heating and holding processes, dispersed rod-like and granular $\delta - Al_2O_3$ oxides, irregular Si–Al–O compounds, and spheroidal SiO_2 particles were formed at the interfacial area because of the selective oxidation and internal oxidation of Al and Si.
2. After the post-holding treatment at 1150 ℃, SiO_2 particles and Si–Al–O compounds successively dissolved into the matrix, and $\delta - Al_2O_3$ oxides were finally transformed into nanoscale $\alpha - Al_2O_3$ oxides. The effect of intragranular residual $\alpha - Al_2O_3$ oxides on the mechanical properties of joints was limited due to their small size and limited amount.
3. The hot-compressed samples were bonded by the migration of newly-formed grain boundaries at the interface. Post-holding treatment further promoted the migration of these boundaries, resulting in a complete healing of the interface.

Acknowledgements This work was financially supported by the National Key Research and Development Program (No. 2018YFA0702900), the National Natural Science Foundation of China (Nos. 51774265 and 51701225), the National Science and Technology Major Project of China (Nos. 2019ZX06004010 and 2017-VII-008-0101), the Strategic Priority Research Program of the Chinese Academy of Sciences (No. XDC04000000), the LingChuang Research Project of China National Nuclear Corporation Program of CAS Interdisciplinary Innovation Team, and Youth Innovation Promotion Association, CAS.

Declarations

Conflict of interest The authors state that there are no conflicts of interest to disclose.

References

[1] S.S. Gill, J. Singh, R. Singh, H. Singh, J. Mater. Eng. Perform. **21**, 1320 (2012)
[2] Y.L. Ji, W. Zhang, X.Y. Chen, J.G. Li, Acta Metall. Sin. Eng. Lett. **29**, 382 (2016)
[3] G. Maizza, R. Pero, F.D. Marco, T. Ohmura, Materials **13**, 2657 (2020)
[4] W.J. Shen, L.P. Yu, H.X. Liu, Y.H. He, Z. Zhou, Q. Zhang, J. Mater. Process. Technol. **275**, 116383 (2020)
[5] X.D. Zhang, C.Y. Deng, D.P. Wang, Z.J. Wang, J.H. Teng, J. Cao, W. Xu, F. Yang, Mater. Des. **91**, 398 (2016)
[6] C. Hai, X.Q. Cheng, C.W. Du, X.G. Li, Acta Metall. Sin. Eng. Lett. **34**, 802 (2021)
[7] G.Q. Chen, Q.X. Yin, G. Zhang, X.H. Wang, B.G. Zhang, J.C. Feng, J. Manuf. Process. **39**, 250 (2019)
[8] L.F. Kanan, B. Vicharapu, A.F.B. Bueno, T. Clarke, A. De, Metall. Mater. Trans. B **49**, 699 (2018)
[9] B. He, L. Cui, D.P. Wang, H.J. Li, C.X. Liu, Acta Metall. Sin. Eng. Lett. **33**, 135 (2020)
[10] H. Li, C. Yang, L.X. Sun, M.Q. Li, J. Alloy Compd. **720**, 131 (2017)
[11] X.W. Yang, W.Y. Li, F. Yang, S.Q. Yu, B. Xiao, Mater. Des. **104**, 436 (2016)
[12] M. Sahin, J. Mater. Process. Technol. **168**, 202 (2005)
[13] M. Mahmoudiniya, A.H. Kokabi, M. Goodarzi, L.A.I. Kestens, Mater. Sci. Eng. A **769**, 138490 (2020)
[14] L. Pan, C.T. Kwok, K.H. Lo, J. Mater. Process. Technol. **277**, 116448 (2020)
[15] Z. Yang, K. Hu, D.W. Hu, C.L. Han, Y.G. Tong, X.Y. Yang, F.Z. Wei, J.X. Zhang, Y. Shen, J. Chen, X.G. Wu, J. Alloy Compd. **764**, 582 (2018)
[16] D.F. Mo, T.F. Song, Y.J. Fang, X.S. Jiang, C.Q. Luo, M.D. Simpson, Z.P. Luo, Adv. Mater. Sci. Eng. **2018**, 8701890 (2018)
[17] K. Mori, N. Bay, L. Fratini, F. Micari, A.E. Tekkaya, CIRP Ann. Manuf. Technol. **62**, 673 (2013)
[18] M.Y. Sun, B. Xu, B.J. Xie, D.Z. Li, Y.Y. Li, J. Mater. Sci. Technol. **71**, 84 (2021)
[19] S. Noh, R. Kasada, A. Kimura, Acta Mater. **59**, 3196 (2011)
[20] G.Q. Chen, Z.L. Feng, J. Chen, L. Liu, H. Li, Q. Liu, S. Zhang, X. Cao, G. Zhang, Q.Y. Shi, Scr. Mater. **128**, 41 (2017)
[21] X. Xu, X.W. Ma, S.B. Yu, G.Q. Zhao, Y.X. Wang, X.X. Chen, Mater. Charact. **167**, 110486 (2020)
[22] C. Zhang, H. Li, M.Q. Li, J. Mater. Sci. Technol. **32**, 259 (2016)
[23] J.Y. Zhang, B. Xu, N.H. Tariq, M.Y. Sun, D.Z. Li, J. Mater. Sci. Technol. **46**, 1 (2020)
[24] L.Y. Zhou, S.B. Feng, M.Y. Sun, B. Xu, D.Z. Li, J. Mater. Sci. Technol. **35**, 1671 (2019)
[25] P. Groche, S. Wohletz, M. Brenneis, C. Pabst, F. Resch, J. Mater. Process. Technol. **214**, 1972 (2014)
[26] Z.C. Zhu, Y. He, X.J. Zhang, H.Y. Liu, X. Li, Mater. Sci. Eng. A **669**, 344 (2016)
[27] N. Sridharan, M. Gussev, R. Seibert, C. Parish, M. Norfolk, K. Terrani, S.S. Babu, Acta Mater. **117**, 228 (2016)
[28] B.J. Xie, M.Y. Sun, B. Xu, C.Y. Wang, D.Z. Li, Y.Y. Li, Mater. Des. **157**, 437 (2018)
[29] H.L. Zhang, X.Q. Chen, B. Xu, M.Y. Sun, D.Z. Li, Metall. Mater. Trans. A **51**, 874 (2020)
[30] Y.P. Wang, Y.H. Liu, S.D. Pay, B. Lan, J. Jiang, J. Mater. Process. Technol. **295**, 117191 (2021)
[31] W.F. Liu, Y.F. Cao, Y.F. Guo, B. Xu, M.Y. Sun, D.Z. Li, Mater. Charact. **169**, 110636 (2020)
[32] B. Jonsson, Scand. J. Metall. **24**, 21 (1995)
[33] B.X. Liu, S. Wang, C.X. Chen, W. Fang, J.H. Feng, X. Zhang, F.X. Yin, Appl. Surf. Sci. **463**, 121 (2019)
[34] K.H. Kim, S.J. Kim, H. Shibata, S.Y. Kitamura, ISIJ Int. **54**, 2144 (2014)
[35] B.J. Xie, M.Y. Sun, B. Xu, C.Y. Wang, J.Y. Zhang, L.Z. Zhao, D.Z. Li, Y.Y. Li, J. Mater. Process. Technol. **283**, 116733 (2020)
[36] C.S. Liu, K.H. Kim, S.J. Kim, J.S. Li, S. Ueda, X. Gao, H. Shibata, S.Y. Kitamura, Metall. Mater. Trans. B **46**, 1875 (2015)
[37] C.H. Shek, J.K.L. Lai, T.S. Gu, G.M. Lin, Nano Mater. **8**, 605 (1997)
[38] A.B. Belonoshko, R. Ahuja, B. Johansson, Phys. Rev. B **61**, 3131 (2000)
[39] J. Chen, Q. Chen, S.J. Qu, H.P. Xiang, C. Wang, J.B. Gao, A.H. Feng, D.L. Chen, Scr. Mater. **199**, 113852 (2021)
[40] T. Kizuka, Phys. Rev. Lett. **81**, 4448 (1998)